

# PCCP

Accepted Manuscript



This is an *Accepted Manuscript*, which has been through the Royal Society of Chemistry peer review process and has been accepted for publication.

*Accepted Manuscripts* are published online shortly after acceptance, before technical editing, formatting and proof reading. Using this free service, authors can make their results available to the community, in citable form, before we publish the edited article. We will replace this *Accepted Manuscript* with the edited and formatted *Advance Article* as soon as it is available.

You can find more information about *Accepted Manuscripts* in the [Information for Authors](#).

Please note that technical editing may introduce minor changes to the text and/or graphics, which may alter content. The journal's standard [Terms & Conditions](#) and the [Ethical guidelines](#) still apply. In no event shall the Royal Society of Chemistry be held responsible for any errors or omissions in this *Accepted Manuscript* or any consequences arising from the use of any information it contains.

## Ordered mesoporous carbons obtained by a simple soft template method as sulfur immobilizers for lithium/sulfur cells

*Noelia Moreno, Alvaro Caballero, Lourdes Hernán, Julián Morales\**

I.U.I. Química Fina y Nanoquímica, Dpto. Química Inorgánica, Campus de Rabanales, Edificio Marie Curie, Universidad de Córdoba, 14071 Córdoba, Spain

*Jesús Canales-Vázquez*

Instituto de Energías Renovables, Paseo de La Investigación 1, Universidad de Castilla-La Mancha, 02071 Albacete, Spain

\* Corresponding author: J. Morales. E-mail: iq1mopaj@uco.es. Fax: 34957218621

### Abstract

Carbon materials with ordered mesopore structures were synthesized using soft template methods and then activated by CO<sub>2</sub> treatment. Sulfur was incorporated in these carbons via a simple chemical deposition method in aqueous solutions and the resulting composites were tested as electrodes in Li-S cells. The electrochemical results showed that well-ordered mesoporous carbons perform better than those with a random mesopore arrangement (wormhole-like mesoporous structure). The mesopore ordering yields a framework of well-connected empty sites that results in an enhancement of both the charge carrier mobility and the reversibility of the electrochemical reaction. Although the activation with CO<sub>2</sub> partially destroys the mesopore arrangement, adverse for the electrode performance, it notably increases the surface area and the micropore content which improves the connectivity between the mesopores. The final observation was an irrelevant effect of the activation process at low current densities. However, at higher rates the activated carbon

composite delivered higher capacities. The hierarchical pore structure formed by micro- and mesopores should guarantee the required fast mobility of the  $\text{Li}^+$ .

## 1. Introduction

Today, lithium-ion batteries play an important role as the primary power source in small-scale applications such as portable electronics. However, their limited energy storage<sup>1</sup> restricts their potential use in applications with larger energetic demands as is the case of electric vehicles or grid scale energy storage systems. For these applications, the reversible chemical reaction of the battery must supply a higher energy density. Sulfur is a promising candidate to meet this requirement as it has the ability to react reversibly with two Li atoms per mole. In other words, its high theoretical capacity ( $1675 \text{ mAh}\cdot\text{g}^{-1}$ ) and specific energy density ( $2600 \text{ Wh}\cdot\text{kg}^{-1}$ ) are notably higher than those of Li-ion batteries based on conventional insertion compound cathodes (around  $500 \text{ Wh}\cdot\text{kg}^{-1}$ ). Another advantage of sulfur is its abundance in addition to its low cost and toxicity. All these promising prospects have attracted a great deal of research efforts to overcome the large problems that affect to the electrodes and electrolytes in the search for satisfactory cell performance<sup>2-4</sup>. One of the main problems of sulfur-based electrodes relates to electronic insulation which severely affects the cell operation. There is a general agreement to mitigate this shortcoming, namely the use of a carbon matrix where S is dispersed. The beneficial effect of carbon is not limited to merely improve the electronic conductivity but also to buffer the volume changes undergone by S and to reduce the loss of the active material by encapsulating the soluble polysulfides within a pore texture. As a consequence there exists a large number of research articles focused on the use of different porous carbons in Li/S batteries<sup>5-47</sup>. In this context, after the pioneering work by Nazar et al.<sup>5</sup>, ordered mesoporous carbons offer promising prospects due to their suitable textural properties such as tunable and uniform pore sizes, large surface areas, and regular pore arrangement. Table 1 summarizes specific capacity values and experimental conditions of different mesoporous carbons used as electrodes for LSB. Most of them have been synthesized by hard template methods using an

inorganic matrix as the porous system generator either  $\text{SiO}_2$ <sup>5, 7,15,19,31,38,47</sup>,  $\text{TiO}_2$ <sup>35</sup> or  $\text{Al}_2\text{O}_3$ <sup>23,42</sup> and the subsequent removal by a chemical treatment which is a serious drawback as the multiple steps required make the procedure complex and tedious. Regarding the capacity values reported, they oscillate in between 500 and 900  $\text{mAh}\cdot\text{g}^{-1}$ , depending on the current density among other parameters.

Recently Xu et al. have described a simple and cleaner synthesis method to produce ordered mesoporous carbon (OMC) through an organic-organic self-assembly strategy using resorcinol and triblock copolymer Pluronic F-127<sup>48</sup>. Moreover, its activation by  $\text{CO}_2$  treatment, a cleaner and less aggressive than KOH treatment, may further increase the surface area and pore volume. Based on these attractive characteristics, herein we examine their applicability to prepare sulfur impregnated electrodes in Li-S battery. These composites exhibited stable, high, reversible capacities ( $\approx 800 \text{mAh}\cdot\text{g}^{-1}$ ) with good cycling efficiency. Furthermore, the activation with  $\text{CO}_2$  in addition to maintain good capacity retention, enhances the electrode rate capability.

## 2. Experimental.

*2.1 Mesoporous carbon (MC) synthesis.* A detailed description of the method can be found elsewhere<sup>48</sup>.  $\text{Na}_2\text{CO}_3$  was dissolved in a formaldehyde solution (37%wt) under stirring in a water bath at about 18°C. Resorcinol was then added for the pre-polymerization and after 1h the solution was mixed with Pluronic F-127 dissolved in ethanol/water followed by the addition of 2M HCl solution. After vigorous stirring for 1 min, the mixture turned white turbid which is an indication of the phase separation. The mixture was stirred 1h and then left standing for 10h to obtain the polymer gel. The polymer gel was dried at room temperature overnight and then was cured at 80°C for 24h in air oven. Two different phases were observed in the gel: the phase in the bottom was an orange transparent solid and the phase in the top was red dust, which was discarded.

The orange transparent solid was carbonized in a tubular furnace at 800°C for 3h under N<sub>2</sub> atmosphere (50mL/min) using a ramp rate of 1°C/min, to get the ordered mesoporous carbon, which was subsequently ball-milled at 300 rpm for 1h. Two mesoporous carbon samples were obtained. The first, named OMC (ordered mesoporous carbon), was obtained by using the same amounts of chemicals as done in ref. <sup>48</sup>. The second, named WMC (wormhole-like mesoporous carbon), was obtained by calcining a larger amount, maintaining the same proportions of chemicals. Then OMC sample was subsequently activated in a tubular furnace at 900°C for 3h under CO<sub>2</sub> atmosphere (50 mL/min) using a ramp rate of 1°C/min. The resulting carbon was named AOMC.

*2.2 Carbon sulfur composites preparation.* All composites were prepared by in-situ sulfur deposition from an aqueous solution of sodium thiosulfate acidified with hydrochloric acid under the following conditions: Na<sub>2</sub>S<sub>2</sub>O<sub>3</sub>·5H<sub>2</sub>O (8.97 g, Sigma Aldrich) was dissolved in H<sub>2</sub>O (500 mL) containing 1% Triton X-100 (15mL, Sigma Aldrich). The solution was mixed with a suspension of the carbon under magnetic stirring. The mixture was heated to 70°C in an oil bath and HCl (12M, 50 mL) was slowly added. The system was kept at this temperature for 15min under vigorous magnetic stirring, cooled to room temperature and kept under magnetic stirring for 24 h. The product was filtered and washed several times with water, ethanol and acetone. Finally, the composites were dried in an air-oven at 80°C overnight. Figure 1 shows a scheme of the different steps followed to obtain the carbon matrix and the composite. They were heated at 180°C under N<sub>2</sub> flow (50 mL/min) during 3h at a heating rate of 5°C/min to facilitate the diffusion of sulfur in the porous system and remove the excess thereof. The composites were named by using the carbon terminology followed by a subscript (h, heated; u, unheated) and the sulfur content.

*2.3 Carbons and composites characterization.* The structural properties of carbons and composites were examined by XRD and TEM. XRD patterns were recorded with a BrukerD8 Advance X-ray diffractometer and the TEM images with a Jeol 2100 electron microscope operating at 200 kV and equipped with an Orius Gatan CCD camera. The sulfur content was determined by

thermogravimetric analysis with a Mettler Toledo-TGA/DSC under nitrogen atmosphere in the 25 to 600°C temperature range using a ramp rate of 5°C/min. The textural properties were determined with a Micromeritics ASAP 2020, using nitrogen as adsorbent.

*2.4 Cell assembly and electrochemical characterization.* Electrochemical experiments were performed on CR2032 coin cells assembled inside an Ar-filled glove box (M-Braun 150 model) with Li metal foil as the counter electrode. To prepare the electrode, sulfur-carbon composites were mixed with Super P carbon black and Polyvinylidenedifluoride (PVDF) binder in a 80: 10: 10 mass ratio in N-methylpyrrolidone (NMP) solution. The slurry was coated onto an aluminum foil current collector using the Dr. Blade technique, then dried in a vacuum oven at 50°C for 24 h. 13 mm diameter disks with a 1.5 mg loading were also dried in a vacuum oven at 50°C for 1h before assembling the cell. The electrolyte was LiCF<sub>3</sub>SO<sub>3</sub> 1M (Sigma Aldrich), LiNO<sub>3</sub> 0.25M (Sigma Aldrich) in 1,3-dioxolane (DOL, Sigma Aldrich) and 1,2-dimethoxyethane (DME, Sigma Aldrich) (1:1 v/v) impregnated in a Celgard polyethylene membrane as separator. The cyclic voltammetry (CV) curves were recorded with Arbin BT2143 at scan rate of 0.10 mV·s<sup>-1</sup> between 3.5 V and 1.0 V. The cycling test were performed on Arbin BT2143 within the potential window 1.6-2.7 V at current density of 100 mA·g<sup>-1</sup>.

### **3. Results and discussion.**

#### *3.1 Structural and textural properties of carbons and composites.*

The structural characterization of the three carbons was inferred from XRD and electron microscopy images. No significant differences were found in the XRD patterns (WAXS mode), Fig. 2. The two broad and weak peak sat ca. 24.5 and 43.4 ° 2θ are typical of highly structural disordered carbons. The low angle region of the patterns (SAXS mode) was more relevant. The OMC showed a strong peak at 0.84 ° 2θ ( $d = 10.5$  nm) associated with porous ordering. This peak was consistent with the results of Xu et al.<sup>48</sup> but insufficient to establish the ordering symmetry. By increasing the

y-scale of the plot, the weak peaks may help to identify more accurately the mesopore-structure symmetry. These peaks can be assigned to reflections belonging to hexagonal and cubic symmetry. By indexing the intense diffraction peak at  $2\theta = 0.84$  the (110) reflection of the body-centered structure (*Im3m* space group), the (200) and (211) reflections are also identified<sup>48</sup>, on the other hand, if the strong peak is indexed as the (100) reflection of a hexagonal structure (*P6mm* space group), the (110) and (200) reflections are distinguished (see insert of Fig. 1b). Thus, XRD pattern suggests that both cubic and hexagonal mesostructures have been formed, in contrast to the results reported by Xu et al. which only described the formation of a hexagonal 2D array<sup>48</sup>. As shown below the two mesostructures can be observed by TEM. The strong diffraction peak of the OMC sample remained in the WMC and AOMC samples but their intensity was lowered, especially for the former sample, which explains the very low intensity reflections, i.e the scale must be enlarged to detect them, and therefore the two symmetries still coexist. In any case, these results suggested that the mesopore ordering in these samples is lowered.

HRTEM images provided a more accurate perspective of the pore arrangement. The images of a significant fraction of particles corresponding to the OMC sample, Fig. 3 a, b, showed the typical stripe-like and hexagonally arranged structure along [110] and [001], respectively and clearly demonstrate the hexagonal mesostructure of this carbon<sup>49</sup>. The cell parameter calculated from the Fast Fourier Transform (FFT) images,  $a = 11.8$  nm is consistent with the (100) reflection in the XRD patterns (Fig. 2). The micrographs also demonstrate that the pore structure is formed by cylindrical mesopores of ca. 3.5 nm in diameter and carbon wall of ca. 7.0 nm in thickness. Nevertheless, a particle minority showed images like that of Fig. 3c with pore arrangement consistent with cubic symmetry. Even in some particles the two arrangements coexist (see Fig. 3d, right side of the arrow, hexagonal arrangement, left side cubic arrangement). Although the coexistence of both cubic and hexagonal mesostructures has been previously suggested<sup>50</sup>, no further evidence was reported to prove this. Therefore, TEM images nicely confirm the results

obtained from the XRD patterns. By contrast, the pore arrangement of WMC was quite different as observed in Fig. 3e, where most of the particles do not show ordered pores. The micrograph reveals that the mesoporous structure consists of spherical pores that form short wormhole-like mesoporous channels with a random orientation. The pore size was estimated to be around 3.4 nm. The random arrangement of the mesopores and the uneven wall thickness may cause the single broader diffraction peak in the XRD pattern, compared with the OMC sample. Similarly, the spacing obtained from the diffuse scattering ring of the FFT image (lower insert of Fig. 3e), ca. 10.6 nm is consistent with the spacing of the diffraction peak of Fig. 2b. To date we have not a clear explanation for the origin of the different pore structure of OMC and WMC samples. Further work is ongoing to establish the mechanism. However, the TEM images revealed a significant difference in the WMC sample, the presence of pseudo-spherical shape particles of about 50 nm in diameter (see Fig. 3e at the right hand side). By increasing the magnification, upper insert of Fig. 3e, these particles were identified as disordered graphitized carbon coming from the precursor systems. This means that the mesoporous arrangement requires very restricted experimental conditions to be attained. Unhomogeneities in the chemical distribution and more probably in the calcination temperatures may explain the difference between the OMC and WMC samples.

The morphological changes originated by the activation with CO<sub>2</sub> were not as drastic as those reported by chemical procedures<sup>51</sup>. A significant fraction of particles lose the pore ordering and the images were similar to those of the WMC sample. A minority fraction either maintained the porous ordering or more commonly ordered and disordered regions (see Fig. 3f). As a consequence one may assume that the carbon particles were not equally attacked and hence this explains the presence of a weaker peak in the XRD pattern compared to the OMC sample (Fig. 2c and d).

The sulfur content in the composites prepared with mesoporous carbons was determined from thermogravimetric data as shown in Fig. 4. The small weight loss observed in pure carbons, more pronounced below 150 °C, was due to sample moisture. The weight loss for the composites

occurred between 180 and 425°C and was assigned to sulfur evaporation. For the unheated composites, sulfur was lost in three steps, the two first barely distinguishable. The weight loss of the higher temperature step was less pronounced and extended over a larger temperature range. Sulfur loss in this step is more strongly bound to the surface<sup>27</sup>. After thermal treatment, the sulfur content decreased between 5 to 10% and its origin was associated with the sulfur loss of the first step as revealed by the TG curves. The sulfur contents will be used to label the composites (for example OMC/S<sub>u</sub>-46, unheated composite made from ordered mesoporous carbon with 46% of sulfur).

The heating treatment also caused a significant change in the sulfur structure. The XRD pattern of the unheated composite OMC/S exhibited well-defined peaks of orthorhombic sulfur (see Fig. 1b). Nevertheless, the carbon maintained the ordered mesoporous structure (see Fig. 2d). On heating the composites, the sulfur (Fig. 2c) low angle carbon peaks (Fig. 2d) disappeared, which is a direct proof of the sulfur amorphization and dispersion into the pores. EDAX analyses of the heated composites were consistent with these results as they revealed a homogeneous distribution of sulfur thorough the carbon particle surface (Fig. 5).

Figure 6 shows the nitrogen adsorption isotherms of the three carbons (in the inset the adsorption isotherm of the composite OMC/S<sub>h</sub>-36 is shown as example). All carbons exhibited a type IV isotherm in the BDDT classification with increasing absorption OMC < WMC < AOMC. The presence of a hysteresis loop in the desorption curve relates to the mesoporous structure of these carbons. The hysteresis shape, between type H<sub>1</sub> and H<sub>2</sub> reveals some connectivity degree between the independent pores via smaller pores (often referred as an ink-bottle pore). This is consistent with the large volume adsorbed at low pressures (from 0.0 to 0.1), associated to the presence of micropores and more pronounced for AOMC as expected. A narrow pore size distribution of 3.6 to 4.1 nm for OMC and AOMC samples respectively, was calculated from the absorption curve based on the BJH model. At low relative pressures, the pore size distribution plots point out the presence of micropores, particularly for the AOMC sample, with average size below 2 nm. The DFT model

(not shown here) corroborated this observation. Table 2 shows selected textural properties of the carbons and the composites. A significant increase of the BET surface area and pore volume were observed on carbon dioxide activation. The  $t$ -plot analysis indicated that a significant fraction of the carbon surface area was associated with the presence of micropores, being this value more pronounced upon carbon dioxide activation. On sulfur loading, the shape of the nitrogen adsorption isotherms changed to type II, typical of non-porous systems, and the surface area values underwent a drastic decrease. This result was not surprising as pure sulfur had an intrinsically low surface area (below  $1 \text{ m}^2 \cdot \text{g}^{-1}$ ). Therefore, both the mesoporous and the microporous system were fully occupied by sulfur, consistent with the electron microscopy images.

### 3.2 Electrochemical properties.

Figure 7 shows the CV curves for OMC/S<sub>u</sub>-46 and OMC/S<sub>h</sub>-36 with a scan rate of  $0.1 \text{ mV} \cdot \text{s}^{-1}$ . The first cathodic scans of both composites are characterized by the presence of a pair of strong peaks at around 2.2 and 1.9 V, consistent with the two steps of the sulfur reduction<sup>2-5</sup>. The first peak is assigned to the conversion of the S<sub>8</sub> molecule into Li<sub>2</sub>S<sub>n</sub> ( $4 \leq n \leq 8$ ) and the second to the rupture of the sulfur chain and eventually to the formation of Li<sub>2</sub>S. In the first anodic process the two expected oxidation peaks overlap and an asymmetric peak is formed centered around 2.7 V due to the high overvoltage needed for the conversion of Li<sub>2</sub>S in Li polysulfide<sup>13</sup>. In the next scan, the reduction peaks tend to shift to lower potentials, somewhat more pronounced for the unheated composite and the oxidation peaks to somewhat higher potentials. The slight increase in the cell polarization together with the decrease in the peak intensities indicate a deterioration of the electrode reversibility in the first few cycles, displayed by a decrease in the capacity values as shown below. Similar comments are valid for the CV curves of the other composites.

To further investigate the electrochemical performance of carbon composites, we carried out galvanostatic cycling performance experiments in coin cells with Li metal as the anode. All the

capacity values are referred to the mass of S. Figure 8 a, b show the discharge /charge profiles of the OMC/S<sub>u</sub>-46 and OMC/S<sub>h</sub>-36 composites between 1.6 and 2.7 V for different cycles. The shape of the discharge/charge curves of the other four composites made from WMS and AOMC both unheated and heated was quite similar. The main characteristic of the first discharge curve was the presence of two voltage plateaus ascribed to the two-step reaction of S with Li during the discharge process. On charging the cell a strong polarization was observed and the plateaus associated to the two reduction steps are worse defined and they overlap, which is consistent with the wide and asymmetric peak that describes the oxidation process in the CV (see Fig. 7). Since pure carbons were electrochemically inert in the potential region used (results not shown), the redox signals were attributed to sulfur. The shape of the subsequent discharge and charges curves was quite similar, except a reduction of the plateau lengths (related with the cell capacity as shown below) and a subtle change in the voltage of both processes, being the latter more cycling-dependent for the heated sample. The cell made from the heated composite (OMC/S<sub>h</sub>-36) delivered a discharge capacity of about 1580 mAh·g<sup>-1</sup>, close to the theoretical capacity of S and notably higher than those of the cells made from the other composites. The capacity values as a function of the number of cycles are shown in Fig. 9 for all the composites studied, together with the coulombic efficiency of the OMC/S<sub>h</sub>-36 composite, taken as example. To ensure the significance of these values they were made in triplicate. After the second cycle, the average value of the coulombic efficiency was around 98%, independent of the composite tested. For a better comprehension of this plot, some values of the discharge capacity are collected in Table 3. As a general comment the cells made from the unheated composites performed worse than those of the heated composites. Sulfur melting improves the connectivity between sulfur and carbon, enhancing the charge carrier mobility and the delivered capacity increases as a result. However, this beneficial effect is offset by sulfur loss (around a 10%). All composites showed a significant capacity loss in the first five cycles, except in the case of OMC/S<sub>h</sub>-36 where the capacity abruptly faded in the second cycle. Nevertheless,

progressive decrease on further cycling causes the leveling of capacity values with those of the AOMC/S<sub>h</sub>-50 composite around 80 cycles. After 100 cycles the capacity delivered by this latter composite was somewhat higher (618 vs. 550 mAh·g<sup>-1</sup>). The composite made from the disordered mesoporous carbon, WMC/S<sub>h</sub>-43, performed worse since the capacity hardly exceeds 450 mAh·g<sup>-1</sup> after 100 cycles.

The increase of sulfur amount (43 versus 36 %), which might block the electron transport paths and the volume to uptake Li<sup>+</sup>, does not seem to be the origin of the performance deterioration since the AOMC/S<sub>h</sub>-50 composite with a 50 % of sulfur even slightly improved the performance. Moreover an increase in the surface area does not appear as a key factor to enhance the electrochemical properties of the mesoporous carbon as the WMC carbon with a higher surface area performs worse than OMC. Nevertheless, both carbons have another significant difference, which is the ordering of the mesoporous system that plays a significant role towards sulfur activation. The mesopore ordering builds a framework of well-connected empty sites available for lodging the sulfur nanoparticles. In addition to the large contact area, this OMC framework facilitates both the electron and ion transports, improving the reversibility of the electrochemical reaction. By contrast, a random mesopore distribution hinders the mobility of the charge carriers and the electrode performance decreases despite the slight increase in the surface area. The activation with CO<sub>2</sub> also partially collapses the mesopore ordering and therefore its effect on the electrochemical properties of the AOMC/S<sub>h</sub>-50 composite should be prejudicial. However, this process causes a significant increase in microporosity, responsible for two beneficial features for the composite performance. The first is the increase in the surface area and pore volume. In addition to host more activated sulfur, it may induce better contact between the electrolyte and the active cathode material. The second is a better connectivity between the mesopores across the microporous system. All these features lead to a better utilization of the active sulfur which alleviates the capacity loss due to the decrease in the mesopore ordering. Compared to the OMC/S<sub>h</sub>-36 composite, the AOMC/S<sub>h</sub>-50

composite shows a lower capacity lower capacity up to the 70 cycle but its better capacity retention makes equal the capacity. On further cycling, this electrode delivers a somewhat higher capacity than that made from OMC/S<sub>h</sub>-36 (see Fig. 9 and Table 3).

The performance of our OMC/S<sub>h</sub>-36 and AOMC/S<sub>h</sub>-50 composites is as good as most of the mesoporous carbons prepared by hard template methods, using either silica, alumina or titania matrix (see Table 1). The ordered mesoporous carbons of ref. <sup>19</sup> deserve a special comment since they were obtained with methods similar to the present study, but with and without a silica matrix. The electrochemical results were quite unexpected, particularly the low capacity value delivered by the carbon obtained without silica source. Apparently, the mesopore ordering in this case seems to play a minor role against other properties such as internal surface or porosity. Anyway, our results are closer to those obtained with tetraethyl orthosilicate as silica source. Independently of pore ordering, other properties such as special morphologies <sup>14,40</sup>, may enhance a better sulfur utilization. Regarding the activation of mesoporous carbons, the use of CO<sub>2</sub> yield better results than those using KOH <sup>7,36</sup>.

The rate capability was tested in these two latter composites which delivered the highest capacity values. The dependence of the capacity upon the current density is shown in Fig. 10. At low rates, it should be noted that the performance of both composites is fairly similar (the observed behavior in prolonged cycling tests). However, at higher rates, the composite made from the activated carbon delivered higher capacities, around 500 mAh·g<sup>-1</sup> at 800 mA·g<sup>-1</sup> compared with 300 mAh·g<sup>-1</sup> delivered by the pristine OMC carbon under the same rate. To the best of our knowledge, the activation of mesoporous structures with KOH, the conventional method to obtain hierarchically micro/mesoporous carbons, improves the electrochemical properties <sup>7</sup>. The main argument used to explain this behavior is based on the assumption of the confinement of short chain-like sulfur molecules (S<sub>2-4</sub>) in the micropores. Compared with the well-known S<sub>8</sub> crown, which should be accommodated in mesopores, these smaller molecules should exhibit a high activity towards

lithiation, the origin of the improved performance. At least at low rates, our data do not match with this model, as the mesoporous ordering is also a beneficial factor for the Li/S reaction. However at high rates a fast  $\text{Li}^+$  migration is necessary to ensure good cell performance. Micropores may favor this condition as they can interconnect the mesopores forming a channel framework to ensure fast mobility of  $\text{Li}^+$ . When the current rate returns to  $100 \text{ mA}\cdot\text{g}^{-1}$ , the electrodes recovered the same capacity values without undergoing a drastic decline, showing again a similar performance at low current rates.

## Conclusions

A rapid synthesis method, which avoids the use of inorganic matrix as template and the subsequent tedious steps to remove it, has been used to prepare ordered mesoporous carbons. By carefully fixing the experimental conditions, highly ordered mesoporous carbons were obtained with complex structures (both hexagonal and cubic mesostructures). The ordering is collapsed by subtle changes in the experimental conditions and the pore system adopts a wormhole-like shape morphology. Also the activation by  $\text{CO}_2$  partially destroys the mesopore arrangement but both the surface area and the micropore content significantly increase. An *in situ* sulfur deposition route was used for preparing sulfur/carbon composites as electrodes for lithium/sulfur batteries. The composites improved their performance by heating at  $180^\circ\text{C}$ , above the sulfur melting point, due to the better contact between carbon and sulfur. The carbons with a well-defined mesopore arrangement yielded better electrochemical responses than that with a random mesopore distribution, attributed to a better connectivity the empty sites available for lodging the sulfur nanoparticles. The performance of the electrode made from the activated carbon was quite similar to that of the ordered carbon despite the partial collapse of the mesopore arrangement after activation. The substantial increase in the surface area and micropore content not only offsets the detrimental effect exerted by the ordering loss but also enhances the electrode rate capability. On the other hand, the capacity values are as good as those reported in the literature for mesoporous carbons obtained by hard template

methods. Therefore, the soft template method used here is an easy strategy to prepare highly pore ordered carbons with good electrochemical properties for lithium sulfur cells.

### Acknowledgements

This work was performed with the financial support of the Ministerio de Economía y Competitividad (Project MAT2011-27110) and Junta de Andalucía (Group FQM-175).

### References

1. R. V. Noorden, *Nature*, 2014, **507**, 26.
2. M. K Song, E. J. Cairns, Y. Zhang, *Nanoscale*, 2013, **5**, 2186.
3. Y. Yang, G. Zheng, Y. Cui, *Chem. Soc. Rev.*, 2013, **42**, 3018.
4. D. Bresser, S. Passerini, B. Scrosati, *Chem. Commun.*, 2013, **49**, 10545.
5. X. Ji, K. T. Lee, L. F. Nazar, *Nat. Mater.*, 2009, **8**, 500.
6. J. Wang, S. Y. Chew, Z. W. Zhao, Ashraf, D., Wexler, J Chen, S. H. Ng, S. L. Chou, H. K. Liu, *Carbon*, 2008, **46**, 229.
7. C. Liang, N. J. Dudney, J. Y. Howe, *Chem. Mater.*, 2009, **21**, 4724.
8. J. J. Chen, X. Jia, Q. J. She, C. Wang, Q. Zhang, M. S. Zheng, Q. F. Dong, *Electrochim. Acta.*, 2010, **55**, 8062.
9. C. Wang, J. J. Chen, Y. N. Shi, M. S. Zheng, Q. F. Dong, *Electrochim. Acta.*, 2010, **55**, 7010.
10. B. Zhang, X. Qin, G. R. Li, X. P. Gao, *Energy Environ. Sci.*, 2010, **3**, 1531.
11. H. Wang, Y. Yang, Y. Liang, J. T. Robinson, Y. Li, A. Jackson, Y. Cui, H. Dai, *Nano Lett.* 2011, **11**, 2644.

12. J. Z. Wang, L. Lu, M. Choucair, J. A. Stride, X. Xu, H. K. Liu, *J. Power Sources*, 2011, **196**, 7030.
13. Y. Cao, X. Li, I. A. Aksay, J. Lemmon, Z. Nie, Z. Yang Liu, Y., *Phys. Chem. Chem. Phys.*, 2011, **13**, 7660.
14. Y. Yang, G. Yu, J. J. Cha, H. Wu, , M. Vosgueritchian, Y. Yao, Z. Bao, Y. Cui, *ACS Nano*, 2011, **5**, 9187.
15. N. Jayaprakash, J. Shen, S. S. Moganty, A. Corona, A. Archer, *Angew. Chem. Int. Ed.*, 2011, **50**, 5904.
16. X. Li, Y. Cao, W Qi, L. W. Saraf , J. Xiao, Z. Nie, J. Mietek, J. G. Zhang, B. Schwenzer, J. Liu, *J. Mater. Chem.*, 2011, **21**, 16603.
17. L. Ji, M. Rao, S. Aloni, L. Wang, E. J. Cairns, Y. Zhang, *Energy Environ. Sci*, 2011, **4**, 5053.
18. L. Ji, M. Rao, H. Zheng, L. Zhang, Y. Li, W. Duan, J. Guo, E. J. Cairns, Y. Zhang, *J. Amer. Chem. Soc.* 2011, **133**, 18522.
19. S. R. Chen, Y. P. Zhai, G. L. Xu, Y. X. Jiang, D. Y. Zhao, J. T. Li, L. Huang, S. G. Sun, *Electrochim. Acta*, 2011, **56**, 9549.
20. R. Elezari, G. Salitra, A. Garsuch, A. Panchenko, D. Aurbach, *Adv. Mater.*, 2011, **23**, 5641.
21. S. Wei, H. Zhang, Y. Huang, W. Wang, Y. Xia, Z. Yu, *Energy. Environ. Sci.*, 2011,**4**, 736.
22. G. He, X. Li, L. Nazar, *Energy. Environ. Sci.*, 2011, **4**, 2878.
23. G. Zheng, Y. Yang, J. J. Cha, S. Hong, Y. Cui, *Nano Lett.*, 2011, **11**, 4462.
24. S. Ever, L. Nazar, *Chem. Commun.*, 2012, **48**, 1233.
25. M. Rao, W. Li, E. Cairns, *J. Electrochem. Commun.*, 2012, **17**, 1.
26. Y. S. Su, A. Manthiram, *Electrochim. Acta*, 2012, **77**, 272.
27. J. Kim, D. J. Lee, H. G. Jung, Y. K. Sun, J. Hassoun, B. Scrosati, *Adv. Funct. Mater.*, 2012, **23**, 1076.
28. Y. S. Su, A. Manthiram,. *Nat. Commun.*, 2012, **3**, 1166.

29. M. Rao, X. Song, E. J. Cairns, *J. Power Sources*, 2012, **205**, 474.
30. S. Dörfler, M. Hagen, H. Althues, J. Tübke, S. Kaskel, M. J. Hoffmann, *Chem. Commun.*, 2012, **48**, 4097.
31. J. Schuster, G. He, B. Mandlmeier, T. Yim, K. T. Lee, T. Bein, L. Nazar, *Angew. Chem. Int. Ed.*, 2012, **51**, 3591.
32. N. Li, M. Zheng, H. Lu, Z. Hu, C. Shen, X. Cang, G. Ji, J. Cao, Y. Shi, *Chem. Commun.*, 2012, **48**, 4106.
33. W. Ahn, K. B. Kim, K. N. Jung, K. H. Shin, C. S. Jin, *J. Power Sources*, 2012, **202**, 394.
34. X. Liang, Z. Wen, Y. Liu, H. Zhang, J. Jin, M. Wu, X. Wu, *J. Power Sources*, 2012, **206**, 409.
35. M. Oschatz, S. Thieme, L. Borchardt, M. R. Lohe, T. Biemelt, J. Brückner, H. Althues, S. Kaskel, *Chem. Commun.*, 2013, **49**, 5832.
36. X. G. Sun, X. Wang, R. T. Mayer, S. Dai, *ChemSusChem*, 2012, **5**, 2079.
37. W. Weng, V. G. Pol, K. Amine, *Adv. Mater.*, 2013, **25**, 1608.
38. L. Yu, N. Brun, K. Sakaushi, J. Eckert, *Carbon*, 2013, **61**, 245.
39. S. Zhao, C. Li, W. Wang, H. Zhang, M. Gao, X. Xiong, A. Wang, K. Yua, Y. Huang, F. Wang, *J. Mater. Chem. A*, 2013, **1**, 3334.
40. X. Zhou, J. Xie, J. Yang, Y. Zou, J. Tang, S. Wang, L. Ma, Q. Liao, *J. Power Sources*, 2013, **243**, 993.
41. X. Tao, X. Chen, Y. Xia, H. Huang, Y. Gan, R. Wu, F. Chen, W. Zhang, *J. Mater. Chem. A*, 2013, **1**, 3295.
42. X. Wang, X. Fang, X. Guo, Z. Wang, L. Chen, *Electrochim. Acta*, 2013, **97**, 238.
43. B. Ding, C. Yuan, L. Shen, G. Xu, P. Nie, Q. Lai, X. Zhang, *J. Mater. Chem. A*, 2013, **1**, 1096.
44. Y. X. Wang, S. L. Chou, H. K. Liu, S. X. Dou, *J. Power Sources*, 2013, **244**, 240.
45. G. Xu, B. Ding, P. Nie, J. Han, X. Zhang, *J. Mater. Chem. A*, 2013, **1**, 4490.

46. K. Xi, S. Cao, X. Peng, C. Ducati, R. V. Kumar, A. K. Cheetham, *Chem. Commun.*, 2013, **49**, 2192.
47. S. Thieme, J. Brückner, I. Bauer, M. Oschatz, L. Borchardt, H. Althues, S. Kaskel, *J. Mater. Chem. A*, 2013, **1**, 9225.
48. J. M. Xu, A. Wang, T. Zhang, *Carbon*, 2012, **50**, 1807.
49. P. Liu, Y. Shi, Y. Wan, Y. Meng, F. Zhang, D. Gu, Z. Chen, B. Tu, D. Zhao, *J. Amer. Chem. Soc.*, 2006, **128**, 11652.
50. D. Long, W. Qiao, L. Zhan, X. Liang, L. Ling, *Microp. Mesop. Mater.*, 2009, **121**, 58.
51. Y. Chen, C. Liu, H.M. Cheng, *J. Porous Mater.*, 2006, **13**, 141.

**Legends of Figures.**

**Figure 1.** Scheme of the different steps followed to obtain the carbon matrix and the composite.

**Figure 2.** (1) WAXS for: (a) OMC; (b) OMC/S<sub>u</sub>-46; (c) OMC/S<sub>h</sub>-36. (2) SAXS for: (a) OMC; (b) AOMC; (c) WMC; (d) OMC/S<sub>h</sub>-36.

**Figure 3.** (a) HRTEM and FFT for OMC along the (110) and (b) (001); (c) HRTEM for OMC spot array with cubic symmetry; (d) HRTEM for OMC two arrangements; (e) HRTEM for WMC and inset of pseudo-circular shape particles and FFT for WMC; (f) HRTEM for AOMC.

**Figure 4.** ATG for: (1) (a) OMC; (b) OMC/S<sub>u</sub>-46; (c) OMC/S<sub>h</sub>-36. (2) (a) AOMC; (b) AOMC/S<sub>u</sub>-60; (c) AOMC/S<sub>h</sub>-50. (3) (a) WMC; (b) WMC/S<sub>u</sub>-56; (c) WMC/S<sub>h</sub>-43.

**Figure 5.** STEM image and elemental map of sulfur in the OMC/S<sub>h</sub>-36 sample.

**Figure 6.** (1) Nitrogen adsorption-desorption isotherm for (a) OMC; (b) WMC; (c) AOMC and the inset of OMC/S<sub>h</sub>-36. (2) Pore size distribution BJH method.

**Figure 7.** CV of a) OMC/S<sub>u</sub>-46 and b) OMC/S<sub>h</sub>-36 composites measured under the potential window of 1.0 - 3.5 V at a scan rate of 0.1 mV·s<sup>-1</sup>.

**Figure 8.** Galvanostatic discharge/charge profiles of OMC/S<sub>u</sub>-46 (a) and OMC/S<sub>h</sub>-36 (b) composite electrodes at 100 mA·g<sup>-1</sup>.

**Figure 9.** Capacity values as a function of the number of cycles for all the composites studied.

**Figure 10.** C-Rate of OMC/S<sub>h</sub>-36 and AMC/S<sub>h</sub>-50.

**Legends of Tables.**

**Table 1.** Summary of Li-S cells made from different meso and micro porous carbons (as reported in the literature)

**Table 2.** Textural properties of OMC, WMC, AOMC and Composites.

**Table 3.** Electrochemical performance of composites (mAh/g-sulfur)

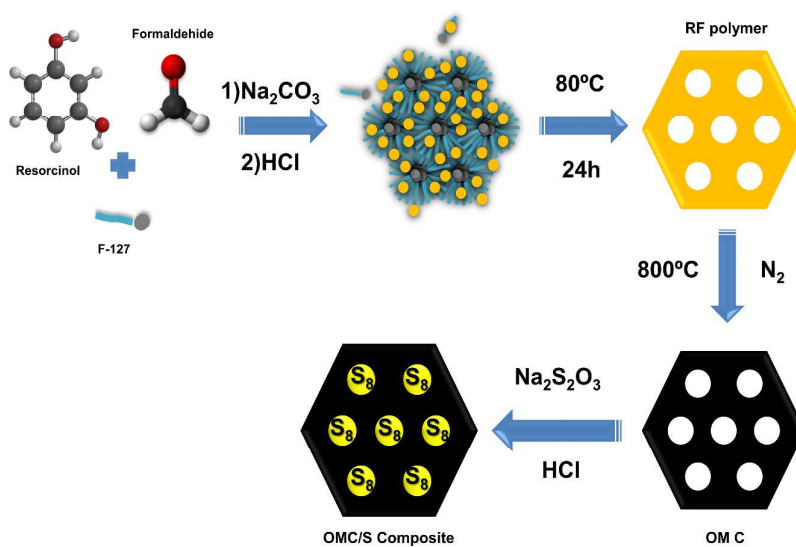


Figure 1

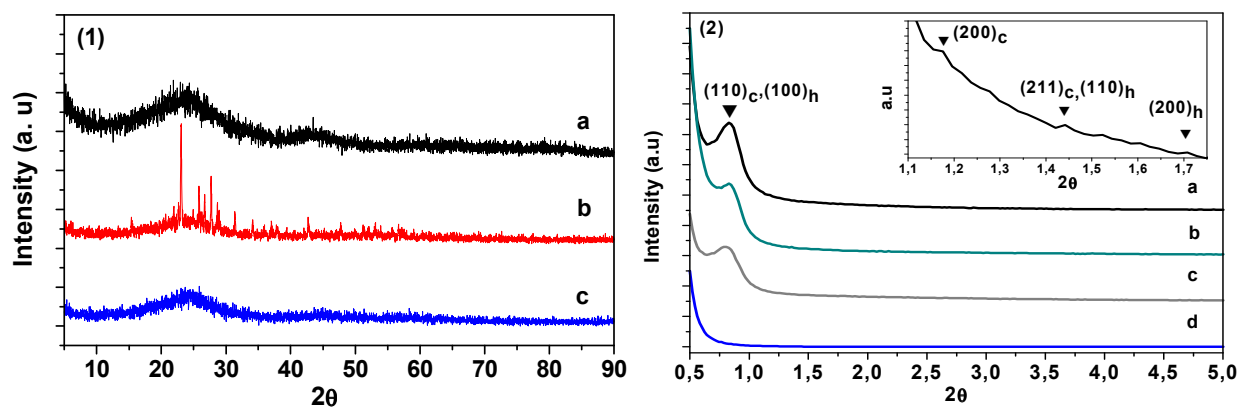


Figure 2

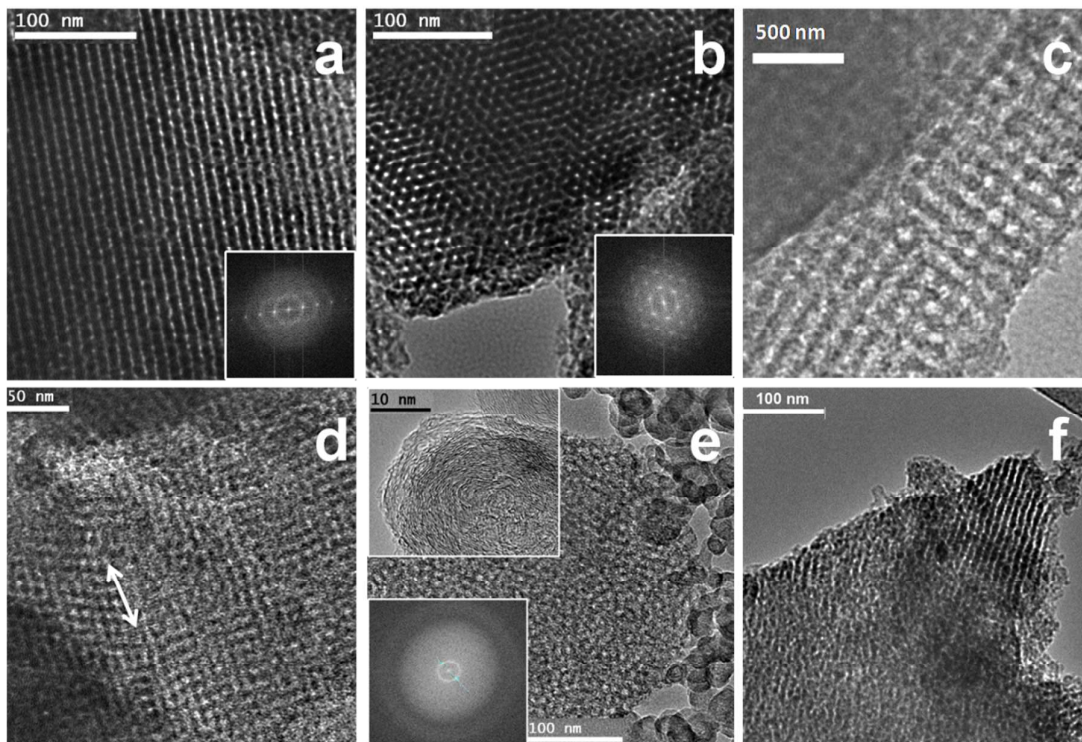


Figure 3

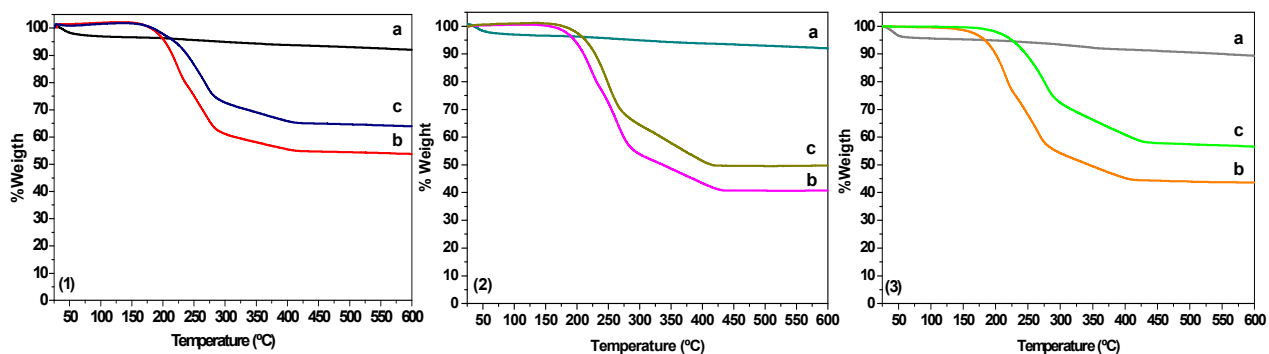


Figure 4

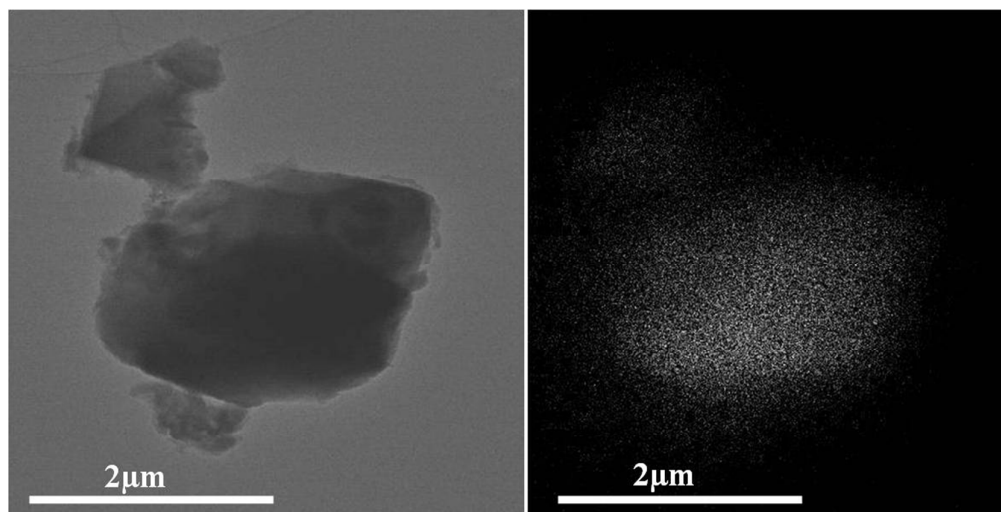


Figure 5

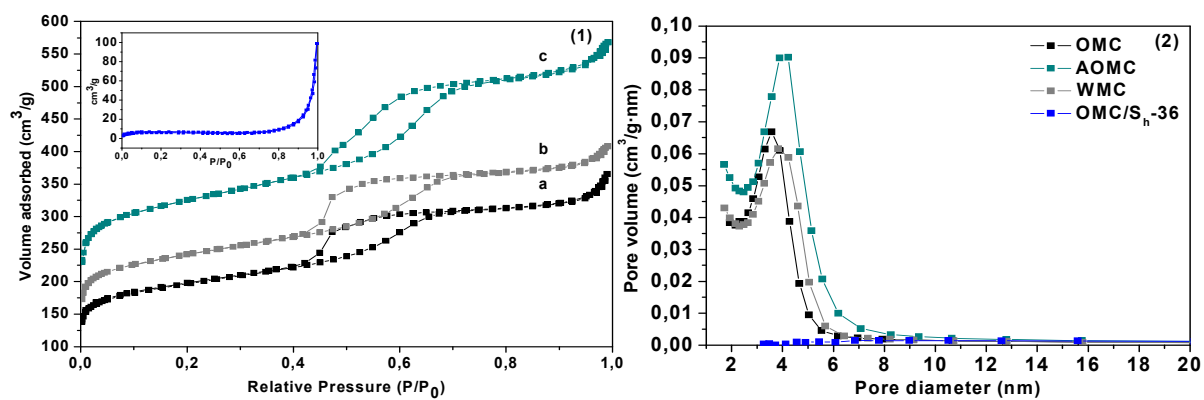


Figure 6

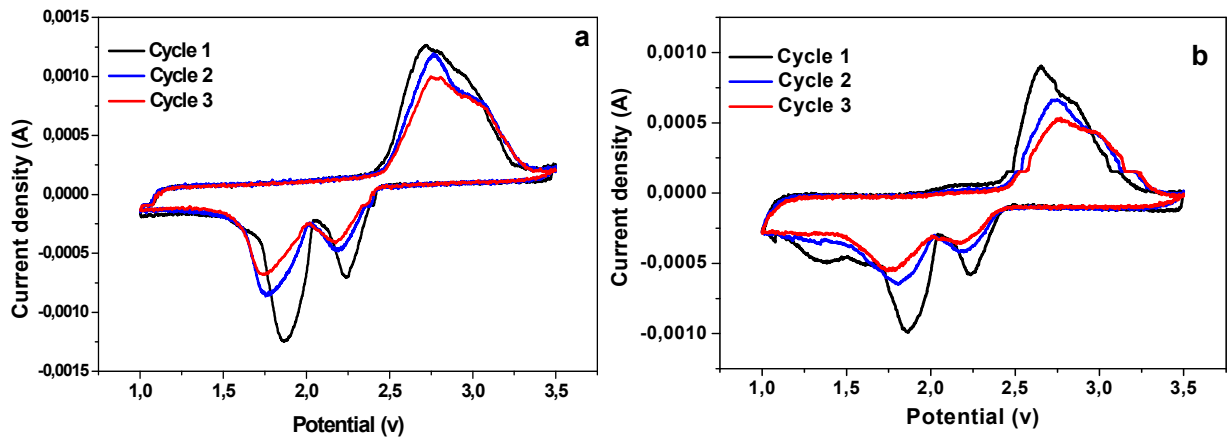


Figure 7

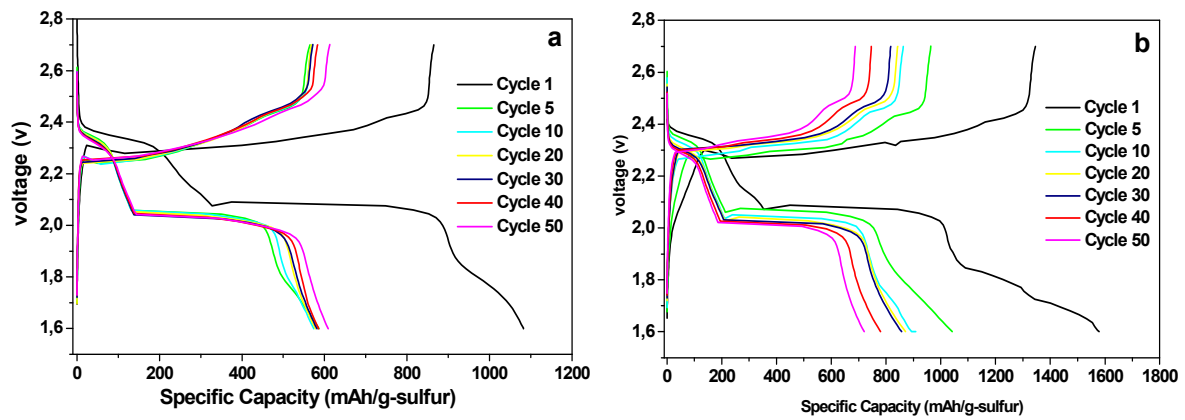


Figure 8

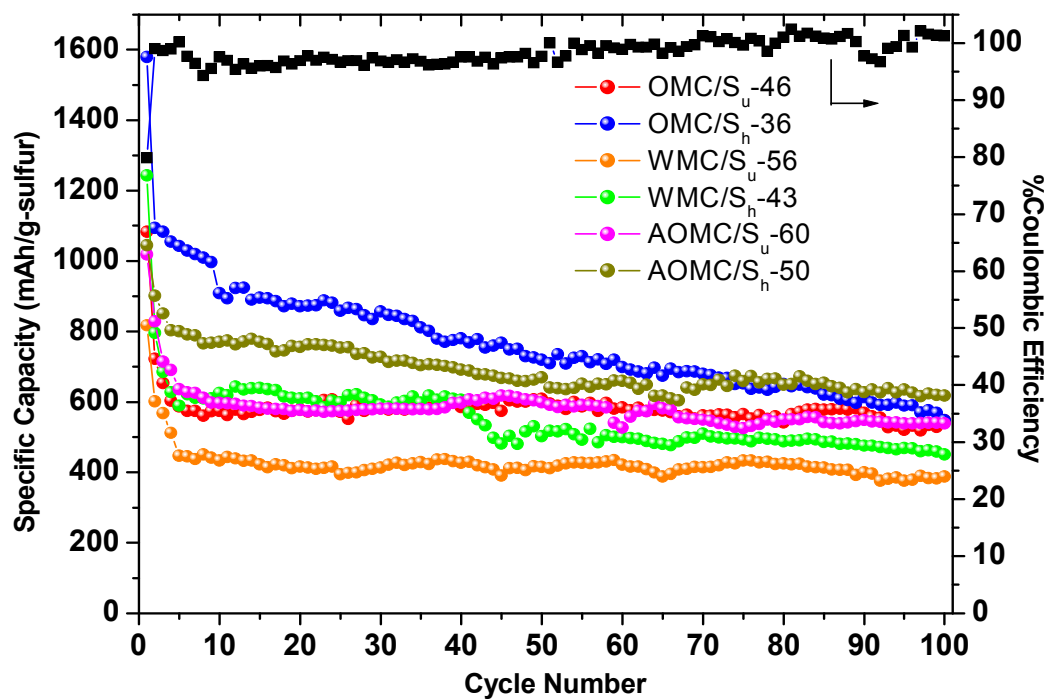


Figure 9

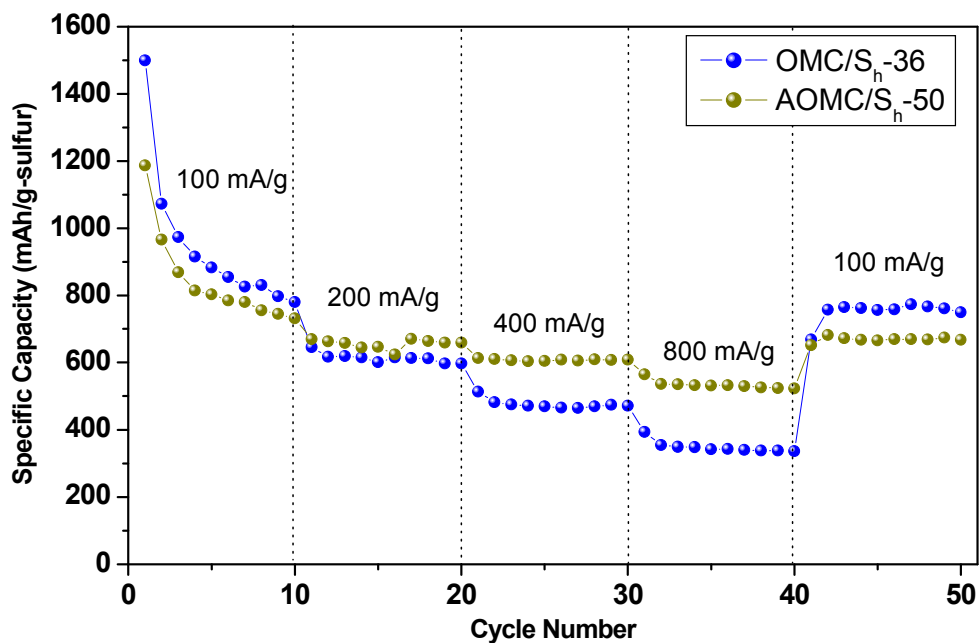


Figure 10

**Table 1** Summary of Li-S cells made from different meso and micro porous carbons (as reported in the literature)

Carbon Type	Ref	Initial Capacity <sup>[a]</sup>	Final Capacity <sup>[a]</sup>	Cycle Number	Rate <sup>[b]</sup>
Highly ordered nanostructured carbon (hard template).	5	1000	750	35	167
Mesoporous carbon further activated with KOH	7	800	250	50	250
Mesoporous carbon coated with a conductive polymer	14	1180	600	160	167
Porous hollow carbon capsules with mesoporous shell structure (hard template)	15	1071	974	100	837
Mesoporous carbon (hard template).	16	1150	600	50	167
Ordered mesoporous carbon prepared from Pluronic F-127 and resol	19				
- without silica matrix		400	250	80	167
- with silica matrix		1138	800	80	167
Hollow carbon nanofiber prepared from anodic aluminum oxide (AAO)	23	1400	730	145	335
Spherical ordered mesoporous carbon prepared from PMMA and silica template.	31	1200	720	100	167
Mesoporous carbon prepared from hard template method with high temperature chlorination titania	35	1038	736	80	167
Mesoporous nitrogen-doped carbon	36	960	600	10	85
Hierarchically porous carbon obtained hydrothermally with the help of silica monoliths	38	980	600	70	167
Highly mesoporous carbon foams prepared from template free Pechini method	41	1217	800	50	84
Hierarchically pore carbon obtained from Al-based porous polymers	42	1200	450	40	167
Hierarchically porous carbon derived from metal organic framework	45	1200	800	50	167
Micro-mesoporous carbide-derived carbon (hard template)	47	1050	600	110	167
[a] Specific Capacity: mAh·g <sup>-1</sup> [b] Rate: mA·g <sup>-1</sup>					

**Table 2** | Textural properties of OMC, WMC, AMC and Composites.

Sample	$S_{\text{BET}}(\text{m}^2 \cdot \text{g}^{-1})$	$V_{\text{T}}(\text{cm}^3 \cdot \text{g}^{-1})$	$V_{\text{MICRO}}(\text{cm}^3 \cdot \text{g}^{-1})$	$S_{\text{MICRO}}(\text{m}^2 \cdot \text{g}^{-1})^*$
OMC	644	0,565	0,174	343
AOMC	1049	0,878	0,322	631
WMC	781	0,631	0,234	457
OMC/S <sub>u</sub> -46	6	0,032	-	-
OMC/S <sub>h</sub> -36	18	0,153	-	-
AOMC/S <sub>u</sub> -60	6	0,031	-	-
AOMC/S <sub>h</sub> -50	26	0,121	-	-
WMC/S <sub>u</sub> -56	4	0,027	-	-
WMC/S <sub>h</sub> -43	9	0,042	-	-

(\*) Values obtained from *t*-plot

**Table 3** | Electrochemical performance of composites (mAh/g-sulfur).

Composite	1 <sup>st</sup>	5 <sup>th</sup>	20 <sup>th</sup>	40 <sup>th</sup>	50 <sup>th</sup>	100 <sup>th</sup>
OMC/S <sub>h</sub> -36	1578	1042	871,5	780,5	720	550
AOMC/S <sub>h</sub> -50	1045	800	756	691	670	618
OMC/S <sub>u</sub> -46	1082	586	578	586	609	548
AOMC/S <sub>u</sub> -60	1018	636	577	598	560	538
WMC/S <sub>h</sub> -43	1243	589	610	606	503	450
WMC/S <sub>u</sub> -56	817	447	416	428	416	388